Influence of Tibetan Plateau autumn snow cover on interannual variations in spring precipitation over southern China

XiaoJing Jia[1] · Chao Zhang[1,2] · Renguang Wu[1] · QiFeng Qian[1]

Abstract

Using observational data from 1979–2015 and a linear baroclinic model (LBM), the present study examined the impact of autumn snow cover (ASC) over the western Tibetan Plateau (WTP) on the subsequent spring precipitation over southern China (SPSC). Focus was placed on the interannual time scale of the snow-precipitation relationship. The ASC over the WTP is positively correlated with the SPSC, and this snow-precipitation relationship is independent of sea surface temperature anomalies over the tropical Indo-Pacific regions. When the ASC over the WTP is more extensive than normal, in the following spring, anomalous southerly winds over eastern China occur and transport water vapor northward from the tropical ocean to the interior of the continent, which is favorable for more SPSC. Further analysis of the energy budget shows that the anomalous ASC over the WTP persists to the following spring because of local positive snow-air feedback. Higher-than-normal ASC over the WTP can cool the above atmosphere and is associated with pronounced negative geopotential height anomalies that dominate in the East Asian-western North Pacific region. These negative height anomalies lead to a weakened and northward-shifted spring East Asian subtropical jet (EASJ). The changes in the spring EASJ lead to divergent anomalies at the upper level over the upstream as well as the central areas of the EASJ; therefore, anomalous low-level convergence and ascent motion dominate over coastal East Asia and in nearby regions, providing a favorable environment for positive SPSC anomalies.

Keywords Autumn snow cover · Tibetan plateau · Southern china · Spring precipitation

1 Introduction

Southern China is an important economic region and the most densely populated region in China. Flooding and drought exert strong influences on the daily lives of millions of people as well as on the economic growth of this region. Numerous works have been devoted to investigating the mechanisms and predictability of summer precipitation over southern China, as compared to other seasons, the summer has more precipitation in this region (e.g., Lau and Li 1984; Chang et al. 2000; Wu et al. 2003; Chen et al. 2013,

You and Jia 2018; Jia et al. 2019). As determined by previous work, the climatological mean spring precipitation can account for more than 30% of the annual total precipitation over southern China (e.g., Feng and Li 2011). Anomalous spring precipitation can also affect the agriculture, economy, transportation, communication and electricity transmission lines. Figure 1a shows that the climatological mean spring (April–May, AM) precipitation peaks over southern China and interannual variations exceeding 50 mm/month. Additionally, over southern China, spring precipitation accounts for at least 60% of the summer precipitation (Fig. 1b).

Many previous works have explored the influence of sea surface temperature (SST) anomalies (SSTAs) over the tropical Indo-Pacific on the spring precipitation over southern China (SPSC) (e.g., Cai et al. 2002; Chen et al. 2003; Wu et al. 2003; Chen and Qian 2005; Feng and Li 2011; Chen et al. 2013; Gu et al. 2018). Wang et al. (2000) revealed that a lower-level anomalous anticyclone forms over the western North Pacific region that is related to the positive winter SSTAs over the central-eastern tropical Pacific and

✉ XiaoJing Jia
  jiaxiaojing@zju.edu.cn

[1] Key Laboratory of Geoscience Big Data and Deep Resource of Zhejiang Province, School of Earth Sciences, ZheJiang University, HangZhou, Zhejiang, China

[2] Department of Atmospheric and Oceanic Sciences and Institute of Atmospheric Sciences, Fudan University, Shanghai, China
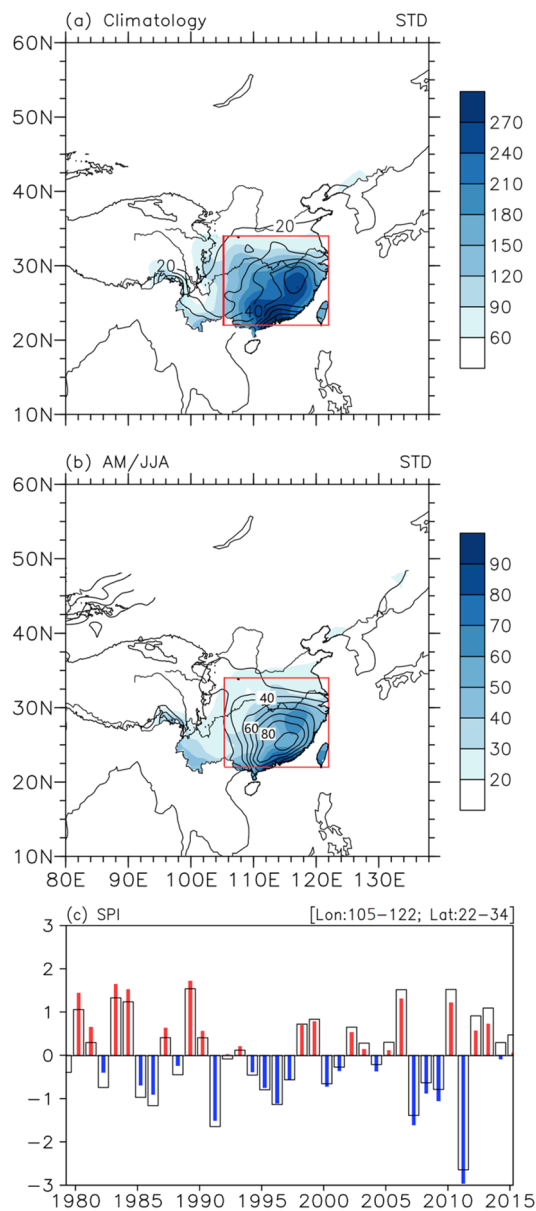
Fig. 1 a Spatial distribution of the spring climatological mean (April–May, AM) precipitation (shading, unit: mm/month) and its standard deviation (contour, unit: mm/month) for the period 1979–2015. **b** Ratio of AM precipitation to summer (June–July–August, JJA) precipitation represented by percentage (contour) and the standard deviation of the interannual components of the AM precipitation (shading, unit: mm/mon). **c** Solid bars represent the normalized spring precipitation index (SPI) of southern China obtained by the area mean of the AM precipitation over the region denoted by the red rectangle box in **a** (105–122° E; 22–34° N), and transparent black bars represent the detrended SPI with the linear trend removed

tropical Indian Ocean. Through local air-sea interactions or the capacitor effect of the Indian Ocean, the anomalous anticyclone can persist to the subsequent summer (e.g., Wang et al. 2003; Xie et al. 2009). Along the western flank of this anticyclonic system, anomalous southerly winds can

transport more water vapor northward from the tropical ocean to the interior of the continent and nearby regions. The SSTAs in the North Atlantic Ocean also promote variations of the SPSC (e.g., You and Jia 2018; Jia et al. 2019). For example, You and Jia (2018) recently revealed that the second empirical orthogonal function (EOF) mode of the SPSC displays a north–south mode that is closely related to the mid- to high-latitude North Atlantic SSTAs in February and March. They further showed that using the dipole SSTAs as a predictor can reasonably improve the seasonal forecast performance of the SPSC.

Other factors, such as snow, can also impact the variation in SPSC. The significant impact of snow on climate variability via the snow albedo effect or hydrological effects is well known (e.g., Dickson, 1984; Watanabe and Nitta, 1998; Kripalani and Kulkarni 1999; Yim et al. 2010; Lin and Wu 2011, 2012; Zuo et al. 2012; Wu et al. 2012a, b; Ye et al. 2015; Cao et al. 2018; Dou et al. 2018). Changes in surface snow cover may modulate surface moisture and local energy fluxes and therefore significantly impact climate locally and surrounding regions (Barnett et al. 1989; Yang et al. 1996; Kripalani et al. 2002; Wu and Qian 2003; Singh and Oh 2005; Wu and Kirtman 2007; Wu et al. 2012a, b, 2016; Lyu et al. 2018; Wang et al. 2019a, b). Diabatic heating associated with anomalous snow cover can act as a driving forcing for the atmosphere and significantly impact climate variations over remote regions (e.g., Lin and Wu 2011, 2012; Wu et al. 2011; Jin et al. 2018; Qian et al. 2019). The influence of extratropical Eurasian snow cover on SPSC variation has been investigated by previous studies (e.g., Wu and Kirtman 2007; Zuo et al. 2012; Jia et al. 2019). The Tibetan Plateau (TP) is the highest elevated plateau on Earth and has the largest amount of semipermanent snow and ice across the midlatitude Eurasian continent (Yeh and Gao 1979; Immerzeel et al. 2010). The processes underlying the impacts of TP thermal forcing on Asian monsoon variations have been extensively studied using both observational data and atmospheric models (e.g., Hahn and Shukla 1976; Khandekar 1991; Zhang and Li, 2004; Dash et al. 2005; Wang et al. 2017, 2018). However, most previous work has explored the influence of winter-spring TP forcing on summer precipitation over East Asia (EA) and nearby areas while the impact of TP forcing on spring precipitation over EA remains unclear. In the current work, we found that the anomalous SPSC is closely related to the changes in snow cover over the TP in the previous autumn. The possible mechanisms responsible for the autumn snow–SPSC relationship were explored via observational data analysis and an atmospheric model. The persistence of anomalous ASC over the WTP has also been examined. Furthermore, most previous work exploring the TP snow effect regards the TP as whole. In a recent work, Wang et al. (2018) revealed that snow cover over different regions of the TP has different

climate impacts. They showed that the anomalous summer snow over the western and southern TP have different climate impacts. In the current work, we also revealed that the TP snow cover that can impact SPSC variation is only limited over the western TP (WTP). In a previous work, Qian et al (2019) revealed that the autumn snow cover over TP has two centers, with one centered over the western TP (centered at 74° E, 36° N) and the other centered over the eastern TP (centered at 94° E, 32° N). Compared to the eastern TP, the climatological mean snow cover over the western TP has larger values. Furthermore, the snow cover over the western TP shows large variation. Therefore, in the current work, the focus is given to the climate impact of snow cover over WTP.

The organization of the remainder of the manuscript is as follows. The datasets, methodology and numerical model are described in Sect. 2. The relationship between the variation of the snow cover over the WTP and the SPSC is presented in Sect. 3. The possible reasons accounting for the persistence of snow over the WTP are investigated in Sect. 4. Finally, the conclusions and a discussion are presented in Sect. 5.

2 Data, methods and numerical model

2.1 Data

The datasets employed in the current work cover the period 1979–2015:

(1) The Northern Hemisphere snow cover extent dataset employed in the current work is from the National Oceanic and Atmospheric Administration (NOAA) climate data record (Robinson et al. 2012). The original weekly snow dataset, which has a horizontal resolution of 25 km for the period from October 1966 to the present, has been obtained from the Rutgers University Global Snow Lab. These snow data were converted to monthly mean data with a 2°×2° latitude–longitude grid resolution.

(2) The monthly mean winds at 850 and 200 hPa, total cloud cover, snow depth, potential vorticity, surface net solar radiation, surface solar radiation downwards, surface net thermal radiation, surface thermal radiation downward and sensible heat flux, and vertical velocity at 500 hPa were obtained from ERA-Interim reanalysis data and gridded at a 0.75°×0.75° resolution (Berrisford et al. 2011).

(3) The Hadley Centre sea ice and SST (HadISST) dataset has a spatial resolution of 1°×1° (Rayner et al. 2003a, b) and is available at https://www.metoffice.gov.uk/hadobs/hadisst/index.html.

(4) The observed daily precipitation data at 824 stations across China were obtained from the China Meteorological Administration (CMA) and converted to monthly mean data.

The Niño 3.4 index was obtained from the Earth System Research Laboratory of NOAA (https://www.esrl.noaa.gov/psd/data/climateindices/list) and used to represent the El Niño–Southern Oscillation (ENSO) variability.

In a previous work, You and Jia (2018) revealed that the characteristics of precipitation in March in southern China bear more similarities to those in the previous February and January than the following April and May; therefore, in the current work, the April–May (AM) precipitation instead of the traditionally used March–April–May (MAM) precipitation was used to represent the SPSC. In southern China, AM is also generally consistent with the time of the first rainy season (e.g., Feng and Li 2011; Gu et al. 2018). The linear trend was removed from the dataset through the regression method because the focus of this work was interannual variations. Pearson correlation analyses were carried out to derive the connection between the two variables. Both regression and composite analyses were used to obtain the spatial structure of a specific field related to an index. Student's t test was applied to assess the significance level of the correlation coefficient.

2.2 Methodology

A phase-independent wave activity flux (WAF), defined from stationary Rossby waves on a zonally asymmetric climatological mean flow, was used to investigate the wave propagation dynamics. The fluxes are parallel to the local group velocity of the stationary Rossby wave. The horizontal component of the WAF definition was given by Takaya and Nakamura (2001) and was calculated by the following equation:

$$W = \frac{1}{2|U|} \begin{pmatrix} U\left(\varphi_x'^2 - \varphi'\varphi_{xx}'\right) + V\left(\varphi_x'\varphi_y' - \varphi'\varphi_{xy}'\right) \\ U\left(\varphi_x'\varphi_y' - \varphi'\varphi_{xy}'\right) + V\left(\varphi_y'^2 - \varphi'\varphi_{yy}'\right) \end{pmatrix}$$

where U = (U, V) represents the zonal and meridional wind velocity components of climatological mean flow, respectively, and ψ denotes the stream function. The primes represent deviations from the time mean, and the subscripts are partial derivatives.

2.3 Numerical model

A detailed introduction of the linear baroclinic model (LBM) used in the current work was provided by Watanabe and Kimoto (2000). Briefly, the spectral baroclinic atmospheric

model employed in the current work is based on primitive equations linearized about the observed climatological state. This atmospheric numerical model was constructed based on a dynamic core of an atmospheric general circulation model (AGCM) cooperatively developed at the Center for Climate System Research (CCSR), University of Tokyo, and the National Institute for Environmental Studies (NIES), Japan. The version of the LBM used in this study has a horizontal resolution of T42 and 20 vertical sigma levels. The LBM has both moisture and dry models, and the dry model was employed in this work.

3 Relationship between the SPSC and ASC over the TP

3.1 Characteristics of the anomalous SPSC-related SCE over the TP

According to Fig. 1a, a spring precipitation index (SPI) is obtained by averaging the precipitation in spring over southern China (105–122° E, 22–34° N) (marked by the red rectangular boxes in Fig. 1a and b), which includes

the region of maximum mean precipitation and year-to-year variability. The SPI is normalized and is depicted in Fig. 1c as solid bars. The current work focuses on the interannual variation in the SPSC; therefore, linear trends have been removed. In the following analysis, the detrended SPI, which is presented as transparent bars in Fig. 1c, is used. To determine the region and season of the TP snow that can be related to the interannual variation in the SPSC, the temporal correlation coefficient (TCC) between the SPI and SCE over the TP is calculated from the previous summer to the current spring, and it is presented in Fig. 2. Simultaneous TCCs are generally not significant over the TP (Fig. 2a). In the previous winter, significant positive TCCs are observed over the WTP and northern TP (Fig. 2b). The most significant TCCs are observed for the previous autumn, when a large area of the WTP is covered by positive TCCs (Fig. 2c). The TCCs over the WTP are generally quite weak and not significant in the previous summer (Fig. 2d). According to Fig. 2c, a snow index is constructed by averaging the SCE anomalies over 30–42° N, 72–80° E (Fig. 2, blue rectangular boxes) to quantitatively measure the variation in snow cover over the WTP that can be related to the SPSC changes.
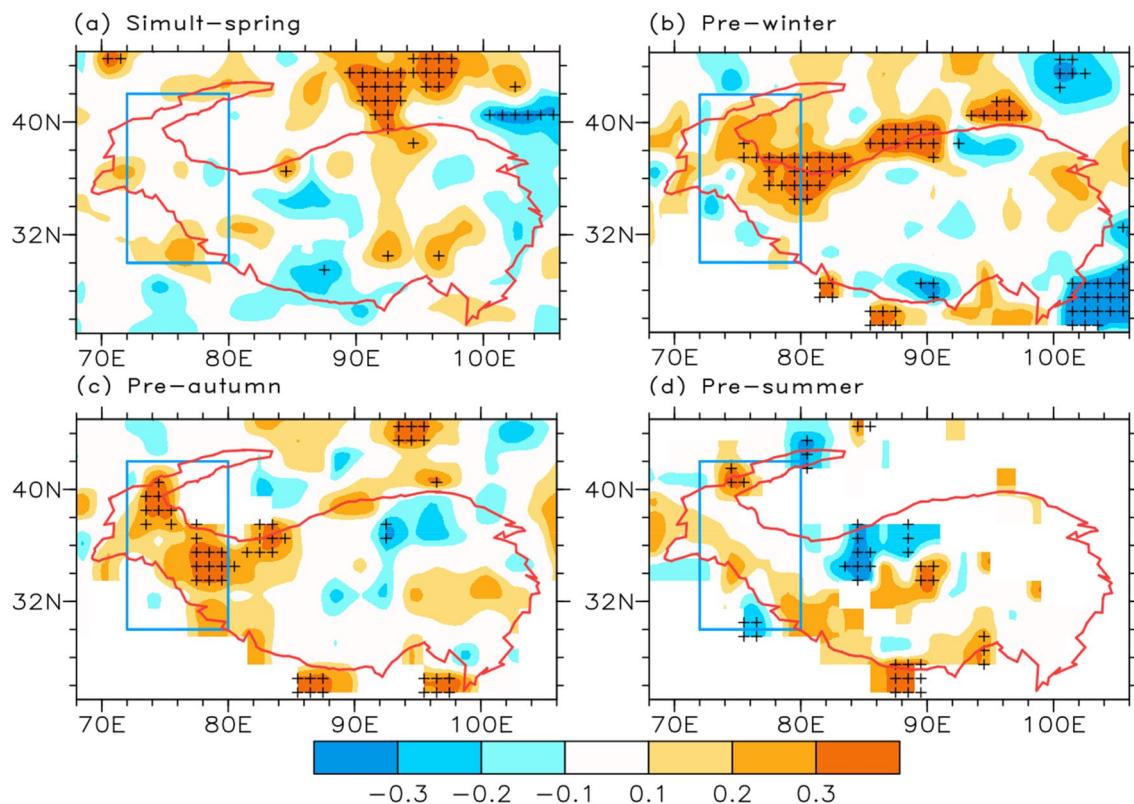
Fig. 2 Correlation coefficient maps of the snow cover extent (SCE) in **a** spring (April–May, AM), **b** the previous winter (December-January–February, DJF), **c** the previous autumn (September–October–November, SON) and **d** the previous summer (June–July–August, JJA) on the SPI. Correlation coefficients significant at the 95% confidence level are denoted by a plus sign. The blue rectangular box denotes the key region of autumn snow cover over the western TP (72–80° E, 30–42° N)
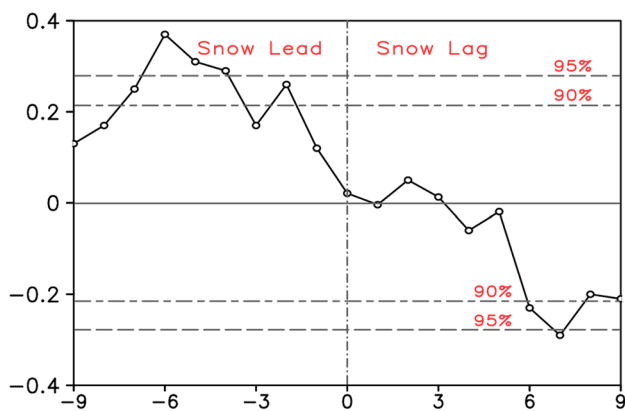
Fig. 3 Lead-lag temporal correlation coefficient between the SPI and snow index (SI) from the previous summer (June–July–August, JJA) to the following winter (December–January–February, DJF). The dashed lines represent the 90% and 95% confidence levels according to Student's t test

The lead-lag correlation between the SPI and the snow index is then calculated from the previous June–July–August (JJA) to the following December–January–February (DJF) and is presented in Fig. 3. These two time series are correlated at a confidence level above 90% from the previous autumn until the previous winter when the changes in the TP snow lead the SPSC, while the correlation is not significant during the simultaneous spring. The most significant TCC is observed in the previous autumn, which is consistent with Fig. 2c, with a TCC of 0.34, and is significant at the 95% confidence level. Figure 3 suggests that the variation in the ASC over the WTP is closely correlated with the SPSC and might be used as a predictor for the SPSC with a lead time up to nearly half a year.

Before we examine the snow-precipitation relationship, first, the characteristics of the autumn snow over the TP are examined. The spatial distribution of the climatological mean ASC over the TP is indicated by the shading in Fig. 4a, and the standard deviation is overlaid as contours. The most expansive maximum ASC is located over the WTP and southern TP, both of which have high altitudes. Figure 4a suggests that the area that is most significantly correlated with the variations in SPSC is also the region with the maximum climatological snow cover and the largest year-to-year variance over the TP. Another maximum center of the ASC can be observed over the central TP, which has also been reported in previous work (e.g., Wang et al. 2018; Qian et al. 2019). The normalized snow index, which is obtained by averaging the ASC in the area marked by the blue rectangular box in Fig. 4a, is displayed in Fig. 4b by solid bars. The snow index displays dominantly positive values before the late 1990s and more negative values during the subsequent period. This trend indicates a decreasing tendency of the snow in autumn over the WTP during
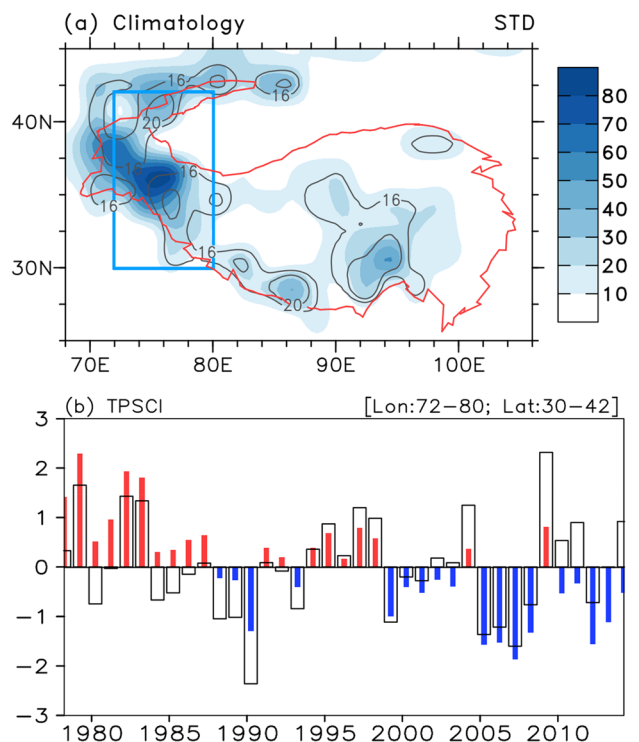
Fig. 4 a Spatial distribution of the autumn climatological mean (September–October–November, SON) SCE (unit: %, shading) and its standard deviation (contour) for the period 1979–2015. **b** Solid bars represent the normalized autumn snow index obtained by the area mean of the SCE over the key snow region denoted by the blue rectangular box in **a** (72–80° E, 30–42° N), and transparent black bars represent the detrended autumn snow index (ASI) with the linear trend removed

the past 40 years, which is consistent with the findings of previous work (e.g., Ye et al. 2015; Wang et al. 2017). The normalized detrended autumn snow index (ASI, hereafter) is represented by transparent bars in Fig. 4b and used in the following analysis to represent the interannual variations in the ASC over the WTP.

Figure 5a presents the regression of the spring precipitation on ASI. Significant anomalous positive spring precipitation appears over southern China, and the largest precipitation anomaly exceeds 30 mm/month. Thus, the result shown in Fig. 5a further confirms that when there is anomalous positive ASC over the WTP, the SPSC is greater than normal. A comparison of Figs. 1a and 5a suggests that the autumn TP snow-related SPSC anomalies account for up to 30% of the total amount of the SPSC, indicating that the ASC over the WTP can explain an important part of the variance in the SPSC. To further confirm the snow-precipitation relationship, we constructed composites of spring precipitation for strong anomalous autumn snow years. If the magnitude of the ASI departs from the corresponding climatology by one standard deviation or more, the year is considered to
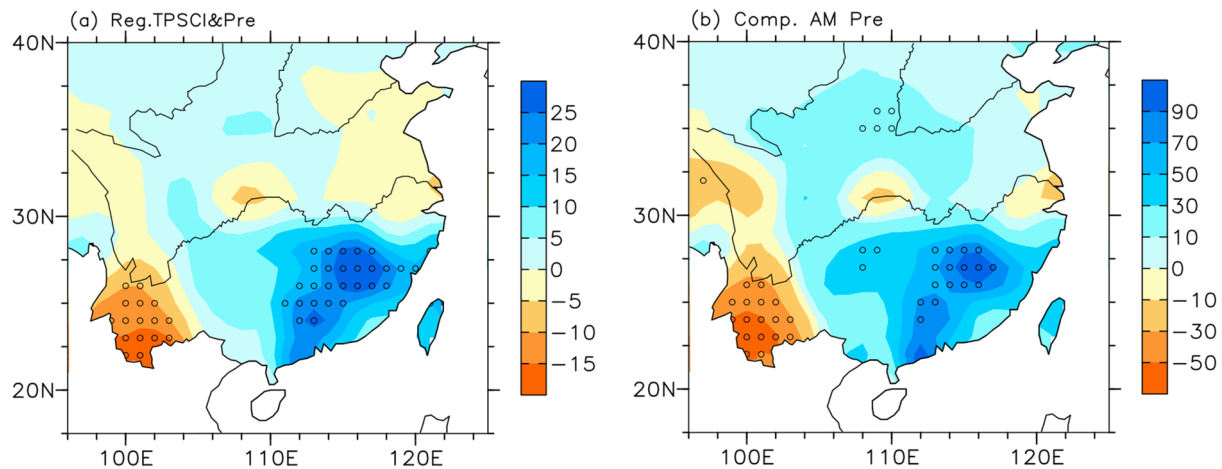
Fig. 5 Spatial distribution of **a** the linear regression map of AM precipitation (unit: mm/month) over southern China onto the ASI for the period 1979–2015. Dotted areas indicate where the correlation coefficients are significant at the 95% confidence level. **b** Composite differences in the AM precipitation over southern China between the high- and low-ASI years for the period 1979–2015. The years that were chosen for the composite are denoted in Table 1

Table 1 Selected years of high ASI and low ASI and their corresponding indices. The selected ENSO and strong SIO years and their corresponding indices are marked by bold and italic fonts, respectively

	Year	Snow Index		Year	Snow Index
High	1979	1.65	**High**	1979	1.65
	1982	**1.43**		*1982*	*1.43*
	1983	1.34		1983	1.34
	1997	**1.20**		*1997*	*1.20*
	2004	1.25		2004	− 1.25
	2009	**2.32**		*2009*	*2.32*
Low	**1988**	**− 1.05**	**Low**	1988	− 1.05
	1989	− 1.02		1989	− 1.02
	1990	− 2.36		1990	− 2.36
	1999	**− 1.13**		1999	− 1.13
	2005	− 1.36		*2005*	*1.36*
	–	–		2006	− 1.22
	2007	− 1.60		*2007*	*− 1.60*

be a strong anomalous snow year. According to this criterion, there were a total of 13 excessive snow years and 13 reduced snow years in the period 1979–2015 (Table 1). The remaining years are defined as normal years. The composite spring precipitation, given in Fig. 5b, clearly shows that in excessive autumn snow years, pronounced anomalous higher-than-normal SPSC occurs. The similarities between Fig. 5a and b further suggest that the snow-precipitation relationship is statistically robust and does not depend on analytical methods.

Before we continue to examine how variations of the ASC over the WTP lead to changes in the SPSC, another issue that needs to be clarified is whether the tropical ocean

contributes to the snow-precipitation relationship. As noted above, studies have suggested that tropical Indo-Pacific SSTAs can impact the SPSC via the western Pacific anticyclone (WPAC) (e.g., Wang et al. 2000, 2003; Feng and Li 2011). The similarity between Fig. 5 and the anomalous precipitation related to WPAC as presented in previous work raises the question as to whether Fig. 5 is a manifestation of only the ENSO-related SPSC variability. To address this issue, tropical SST anomalies associated with the ASI from autumn to the following spring, obtained by regression, are presented in Fig. 6. In association with the positive WTP snow anomalies in autumn, noticeable positive SST anomalies occur in the central-eastern tropical Pacific and with the magnitude peaking two months later (Fig. 6b) and persist until spring (Fig. 6d). Pronounced anomalous positive SST can also be noticed in the southern Indian Ocean during January–February–March (JFM) (Fig. 6c) and can even be observed in the following spring (Fig. 6d). The above results suggest that the evolution of anomalous ASC over the WTP is accompanied by changes in the tropical Indo-Pacific SSTAs.

To exclude the influence of the SSTAs over the tropical Indo-Pacific Ocean on the snow-precipitation relationship, two SST indices are used to represent the SST variation over the eastern tropical Pacific and the Indian Ocean, e.g., the Niño 3.4 index in November–December–January (NDJ) and a Southern Indian Ocean SST index (SIO), which is obtained by averaging the JFM SSTAs over the areas represented by the blue rectangle in Fig. 6c. El Niño (La Niña) events are selected if the Niño 3.4 index is greater (less) than 0.8 (− 0.8) of a standard deviation. Similarly, warm (cold) Indian SST years are defined when the SIO is greater (less) than 0.8 (− 0.8) of a standard deviation. Composites of
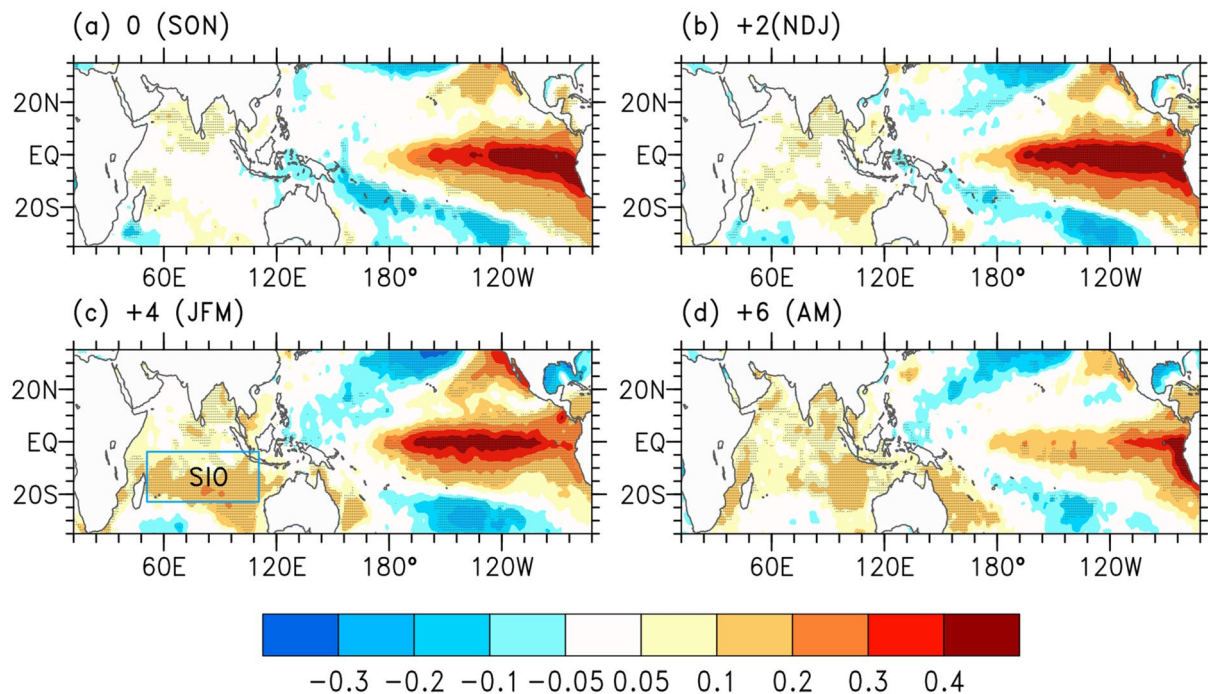
Fig. 6 a Spatial distribution of the linear regression maps of SST (unit: °C) onto the ASI for the period 1979–2015 for **a** SON, **b** NDJ, **c** JFM and **d** AM. Correlation coefficients significant at the 95% are dotted. The blue rectangular box denotes the key region of the SST anomalies over the southern Indian Ocean (50–110° E, 5–25° S)

spring precipitation for strong snow years with both El Niño and La Niña years removed (Fig. 7a) or both warm and cold Indian SST years removed (Fig. 7b). Figure 7c presents the composite precipitation of strong snow years with both El Niño and La Niña years and warm and cold Indian SST years removed. A comparison between Figs. 5 and 7a–c shows many similarities in the spring precipitation anomaly patterns, indicating that the TP snow-SPSC relationship is independent of the SSTAs over the tropical Indo-Pacific region.

3.2 Relationship between the atmospheric circulation anomalies and TP snow

To understand the link between the variation in the ASC over the WTP and the SPSC anomalies, the ASI-related changes in the low-level atmospheric circulation anomalies in spring are depicted in Fig. 8. During years when the ASC over the WTP is greater than normal, in the following spring, pronounced negative and positive geopotential height anomalies are observed over EA and the western North Pacific (Fig. 8a), indicating a weakened land–ocean pressure contrast during this season that can result in weaker northerly winds from the interior high-latitude regions. This is confirmed by anomalous southwesterly winds at 850 hPa over coastal EA, as shown in Fig. 8b. These anomalous southerly winds bring warm water vapor from the tropical ocean to the interior of the continent,

causing a convergence of moisture over southern China, which is favorable for more spring precipitation (Fig. 8c).
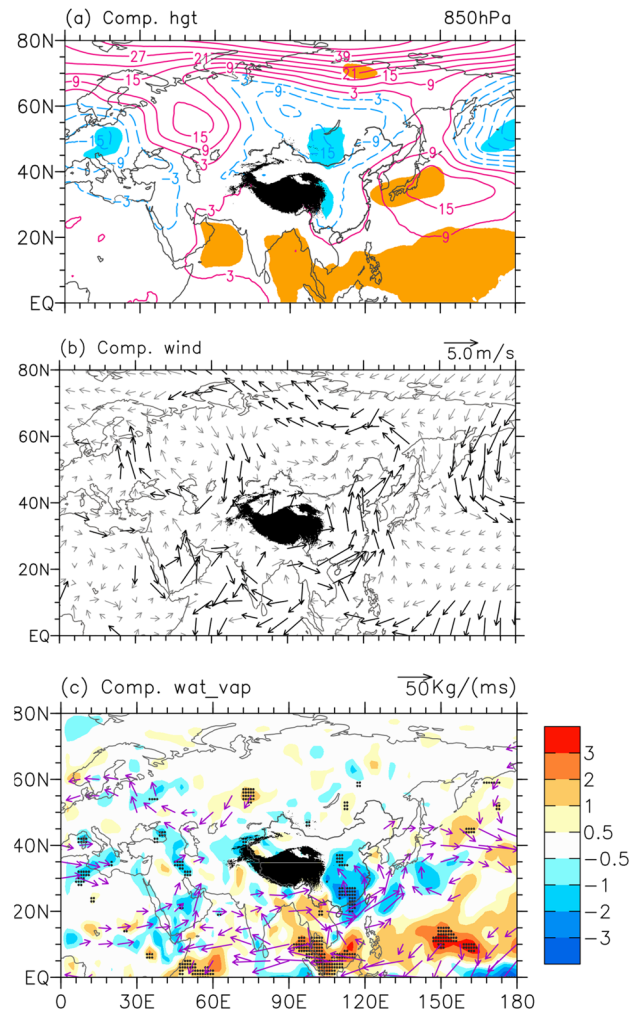
The ASI-related atmospheric circulation anomalies are also significant in the mid-troposphere, where the two anomalous centers of geopotential height over the EA-western North Pacific can also be clearly noticed at 500 hPa (not shown). In the upper troposphere, climatologically, there is a maximum zonal wind band along 30° N, which is referred to as the East Asian subtropical jet (EASJ), which attains wind speeds of 70 m/s at 200 hPa in winter with its center located to the east of Japan. In spring, the maximum climatological zonal wind around the EASJ core is weaker than that in winter but still reaches 45 m/s (Fig. 9, yellow shading). Associated with positive anomalous snow cover over the WTP, there is a weakening and a northward shift of the EASJ. The entrance of the EASJ is an upper-level convergence zone (e.g., Yang et al. 2002). The weakening of the EASJ over this region can cause anomalous divergence in the upper troposphere. Anomalous convergence in the lower troposphere and anomalous upward motion will follow. The composite maps of the divergence at 850 hPa and the vertical velocity at 500 hPa are calculated and presented in Fig. 10. It can be seen that low-level anomalous convergence (Fig. 10a) and anomalous upward motion (Fig. 10b) dominate eastern and southern China. The anomalous ascent motion, together with the anomalous southerly wind
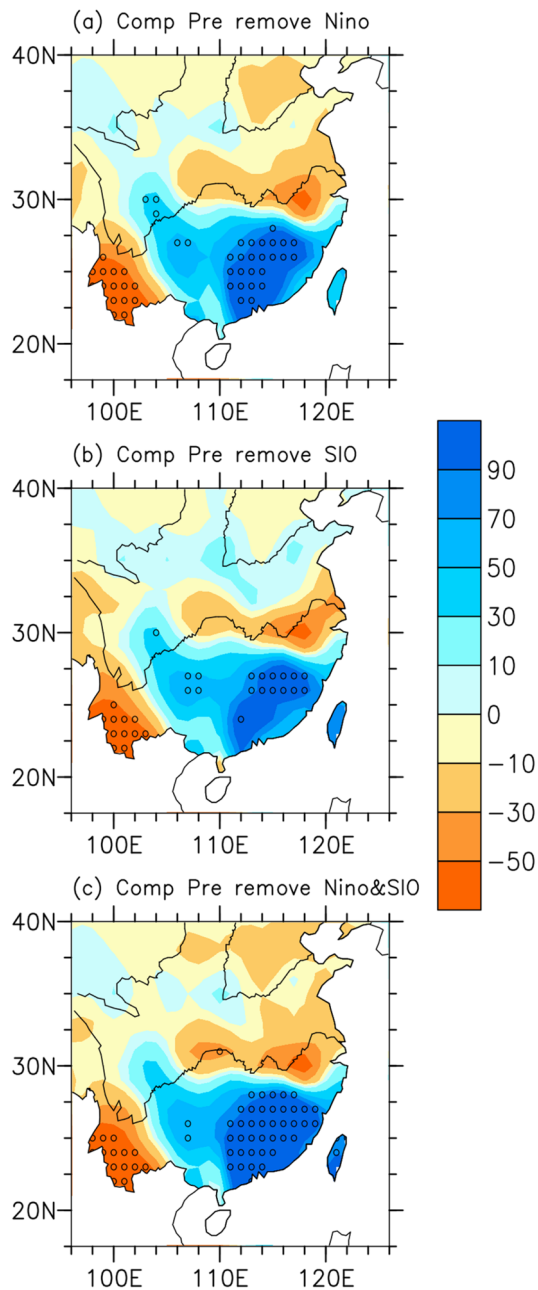
Fig. 7 Composite differences in AM precipitation (unit: mm/month) between high and low ASI years for the period 1979–2015 **a** without strong ENSO years, **b** without strong SIO years and **c** without either strong SIO or ENSO years. The strong ENSO years and strong SIO years are marked with red and blue fonts, respectively, in Table 1. Dotted areas indicate where the precipitation anomalies are significant at the 95% confidence level

Fig. 8 Composite differences between high- and low-ASI years for the period 1979–2015 for **a** Z850, **b** 850-hPa wind (mm/day) and **c** vertical integrated water vapor transport (vector, unit: kg/(ms) from surface to 300-hPa and divergence (shading, 10^{-1} mm/s) in AM. Shaded areas in (**a**) and dotted areas in (**c**) indicate the areas where the anomalies are significant at the 95% confidence level. The contour intervals are 6 m for (**a**). The dark black vectors in (**b**) represent wind anomalies that are significant at the 95% confidence level

from the low-latitude ocean (Fig. 8c), forms a favorable condition for positive SPSC anomalies.

To further understand how snow forcing over the WTP impacts the SPSC, the LBM model is used in this section to conduct numerical experiments. The TP is the highest land mass on Earth, 4000 m above sea level on average.

Anomalous snow cover at the TP surface acts as an atmospheric diabatic cool forcing in the troposphere (e.g., Wang et al. 2019a, b; Qian et al. 2019). Following previous work (Wang et al. 2018), an idealized convergence forcing is set over the WTP (Fig. 11a). The idealized forcing has an elliptical horizontal shape centered at 37° N, 75° E. The forcing has a uniform distribution in the vertical direction. This convergence forcing is set to mimic the effect of the WTP snow forcing on the local atmosphere. The climatological autumn mean flow for the period of 1979–2015 is used in the model experiments. The idealized thermal forcing is switched on at the first day of the integration and persists throughout the model integration. The model response of the wind at
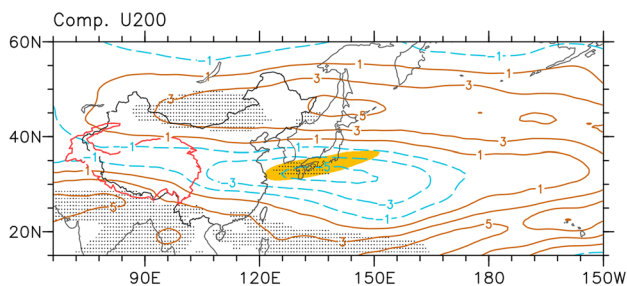
Fig. 9 Composite differences in zonal wind at 200 hPa (unit: m/s) in AM on the ASI for the period 1979–2015. The yellow shading denotes the climatological position of the jet core with a zonal wind greater than 43 m/s. The dotted regions represent anomalies significant at the 95% confidence level

850 hPa (vectors) and the geopotential height at 150 hPa (shading) averaged over days 15–20 is depicted in Fig. 11b, and the zonal winds is depicted in Fig. 11c. They reflect a steady atmospheric response to the prescribed forcing.

Figure 11b shows that after 2 weeks of forcing, in the upper troposphere, the WTP is under the control of an anomalous low geopotential height system. Meanwhile, pronounced anomalous low-level southerly winds dominating

eastern EA can bring water vapor from the tropical ocean to the continent as well as nearby regions and might contribute to more precipitation over southern China. A comparison between Figs. 9 and 11c shows that the weakening of the EASJ is also clearly seen from the model output. In general, the spatial structure of the model circulation response bears reasonable similarities to that in the observations, suggesting that although differences can be noticed, the numerical experiment results confirm that the TP autumn snow forcing over the WTP may impact the SPSC variation through changing the atmospheric circulation around EA-western North Pacific areas.

4 Persistent impact of ASC over the WTP

In the last section, we identified a cross-season relationship between the ASC over the WTP and the SPSC. However, the question that needs to be clarified is how the impact of the anomalous autumn snow could persist until the following spring. To shed light on the possible cross-season snow-precipitation linkage, the time evolution of the snow anomalies over the WTP from autumn to the subsequent spring is examined. Figure 12 shows the ASI-related snow cover and

Fig. 10 The composite differences in **a** wind divergence at 850 hPa (unit: 10^{-7} s^{-1}) and **b** vertical velocity at 500 hPa (unit: 10^{-2} Pa/s) in AM on the ASI for the period 1979–2015. Dotted areas indicate where the anomalies are significant at the 90% confidence level
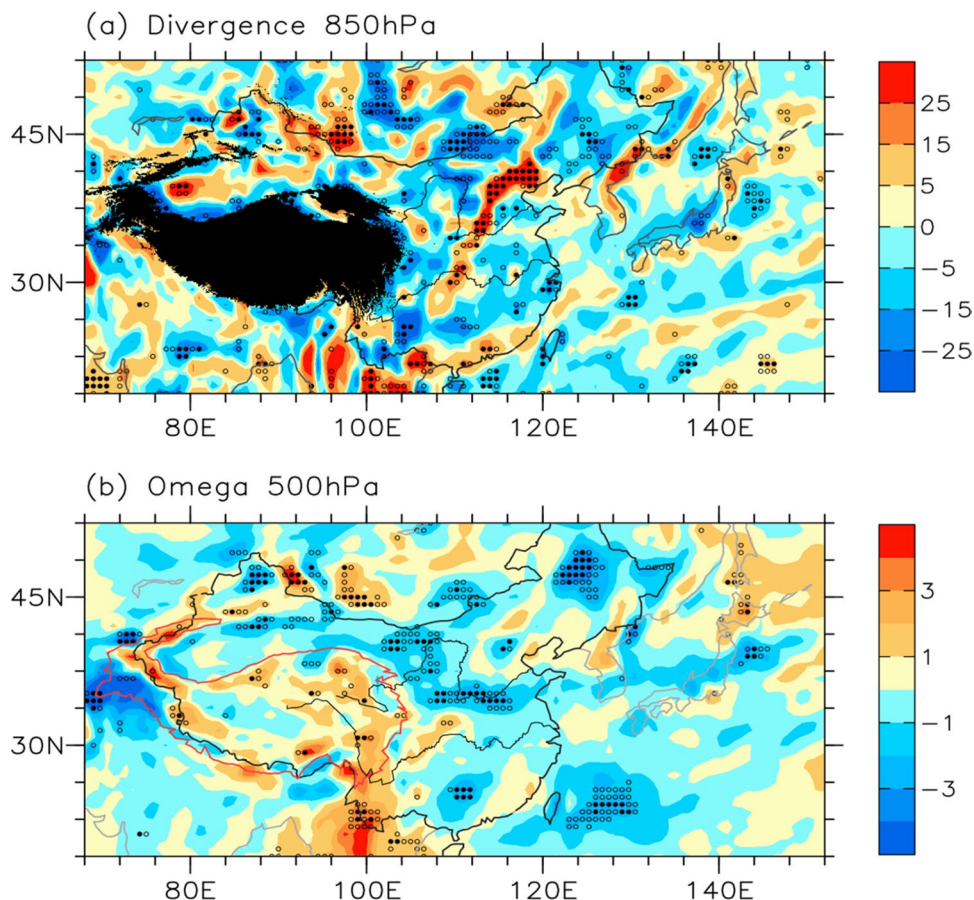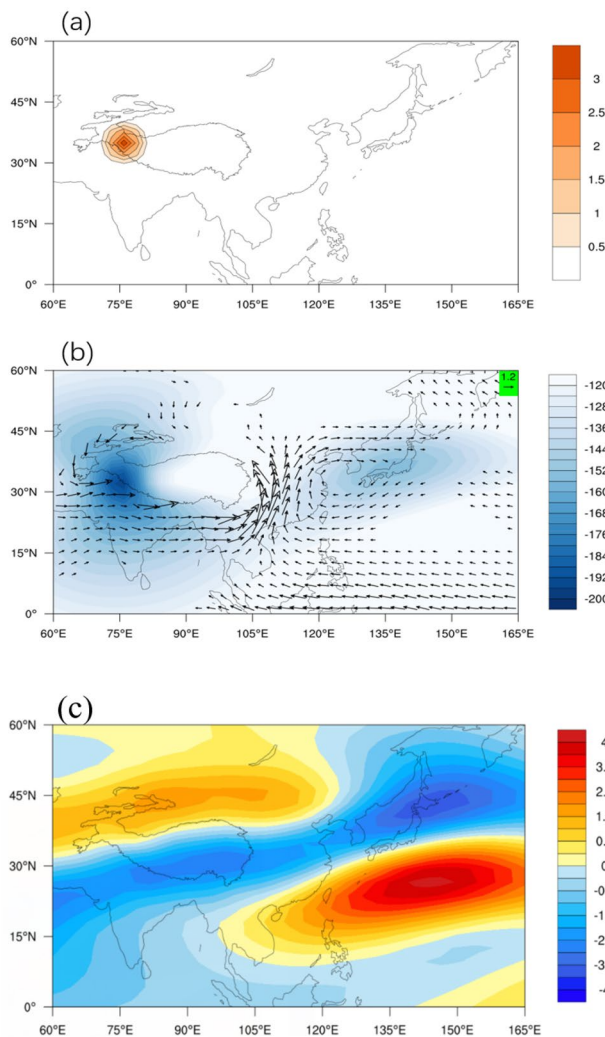
Fig. 11 a Spatial distribution of the convergence forcing for the numerical experiments **b** model response of geopotential height at 150 hPa (unit: m, shadings) and the horizontal winds at 850 hPa (m/s; vectors) and **c** zonal winds at 150 hPa (unit: m/s, shadings) averaged over days 15–20. The scale for winds for (**b**) is shown at top-right corner

snow depth anomalies obtained by regressing these variables on the ASI. Pronounced positive snow cover and snow depth anomalies are observed over the WTP from autumn to the following spring.

It is known that autumn is the season for TP when snowfall starts and that the snow depth is not large in autumn. During this period, the SCE anomalies are large, while the snow depth anomalies are small (Fig. 12a, e). In the following winter, the snowfall accumulates, and the snow depth increases with time. In this case, snow depth anomalies could be large, while snow cover anomalies are small, as addition or removal of snow only changes the snow depth (Fig. 12b, f, c, g). In spring, the snow cover anomalies become large again as the snow depth reduces

rapidly due to the increased temperature (Fig. 12d, h) (e.g., Wu et al. 2016). The persistence of these snow anomalies over the WTP suggests the continuous influence of snow on the above atmospheric circulations. In a previous study, Wang et al. (2019a, b) showed that the central-eastern TP snow cover anomalies have high month-to-month persistence during October through April. Here, we further revealed that the anomalous snow over the WTP also has good persistence during the cold season. An examination of the temporal correlation coefficients of ASI and the snow index of the following seasons shows that the temporal correlation coefficients are 0.35 and 0.28 for early winter and spring, significant at the 90% confidence level, consistent with previous work (Wang et al. 2018).

To understand the mechanisms of the persistence of WTP ASC during the cold season, the anomalous potential vorticity, vertical velocity and total cloud cover associated with the ASI are examined (Fig. 13). In summary, as revealed by previous work (e.g., Wang et al. 2018; Jia et al. 2018), the underlying anomalous snow can cool the overlying atmosphere, which will result in tropospheric anomalous negative geopotential height. On the other hand, Hoskins et al. (1985) indicated that upper-level anomalous negative height and cold temperatures may generate positive potential vorticity anomalies in the upper level, as shown in Fig. 13a–d. Then, anomalous vertical motions (Fig. 13e–h) and positive anomalous cloudiness (Fig. 13i–l) occur, which lead to increased snowfall over the WTP. This positive snow-air feedback persists from autumn to the following spring and may help to maintain the excessive snow cover over the WTP.

The cross-section of the ASI-related winds and geopotential height anomalies along 32.5° N, obtained by regression on the ASI from autumn to the following winter are presented in Fig. 14 to show the evolution of the anomalous atmospheric circulation related to ASC variations. In autumn, anomalous negative geopotential height appears over the plateau and extends to the upper troposphere. The most significant negative geopotential height anomalies are observed above the WTP (Fig. 14a), which is consistent with previous work (Wang et al. 2018; Jia et al. 2018; Qian et al. 2019). The negative geopotential height anomalies increase in magnitude with increasing altitude and reach a maximum at 300 hPa. Ascending motion can also be observed in the WTP. In the following winter and spring, circulation anomalies intensify in magnitude with time, forming a pronounced band of negative geopotential height anomalies that expands from the WTP to the western North Pacific (Fig. 14b, c). The cross-section of the ASI-related winds and geopotential height anomalies averaging between 22° N and 34° N is also examined (not shown). Significant ascending motion can be observed to the east of the TP in AM, favorable for more than normal precipitation over southern China, consistent with Fig. 10.
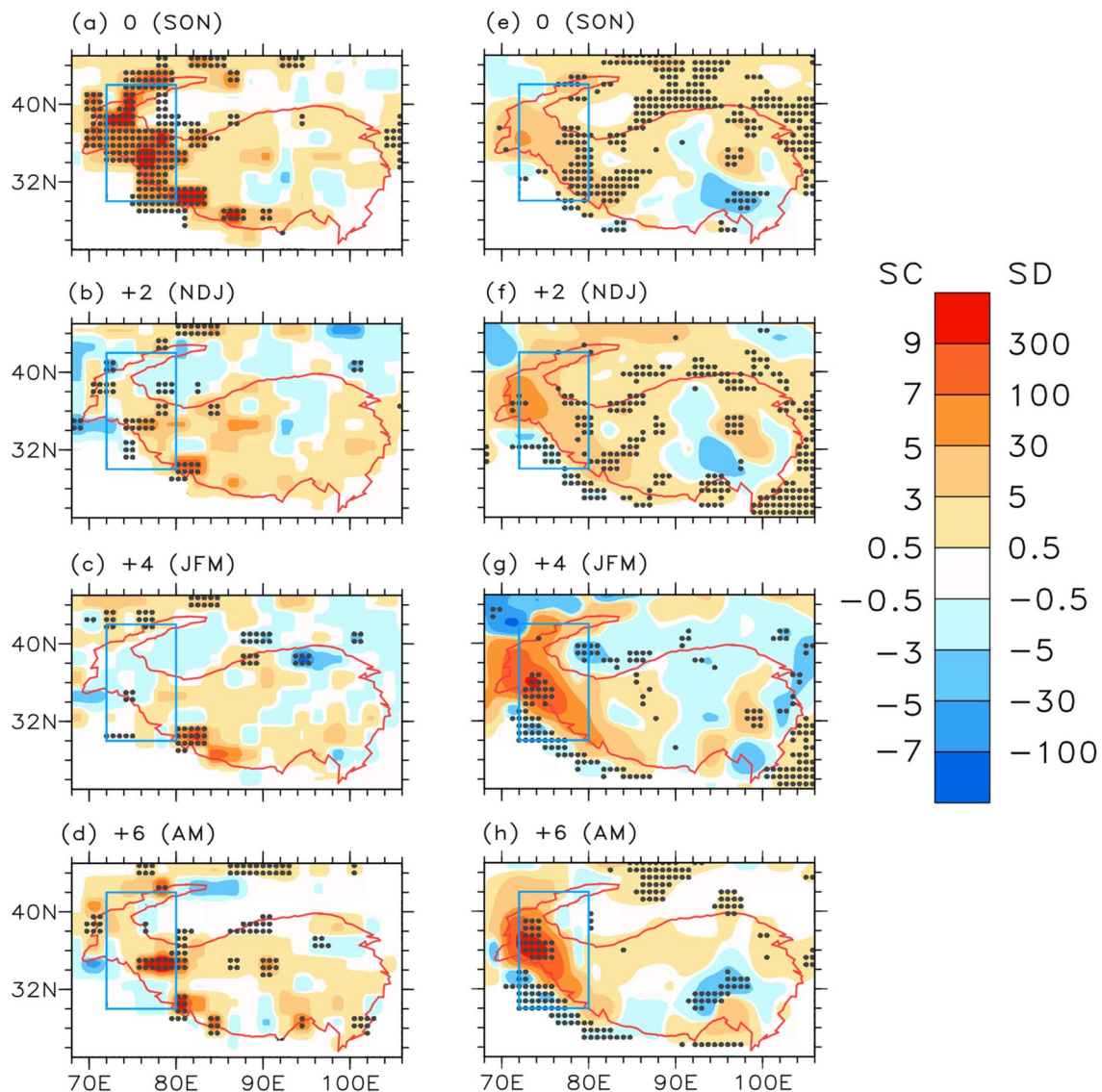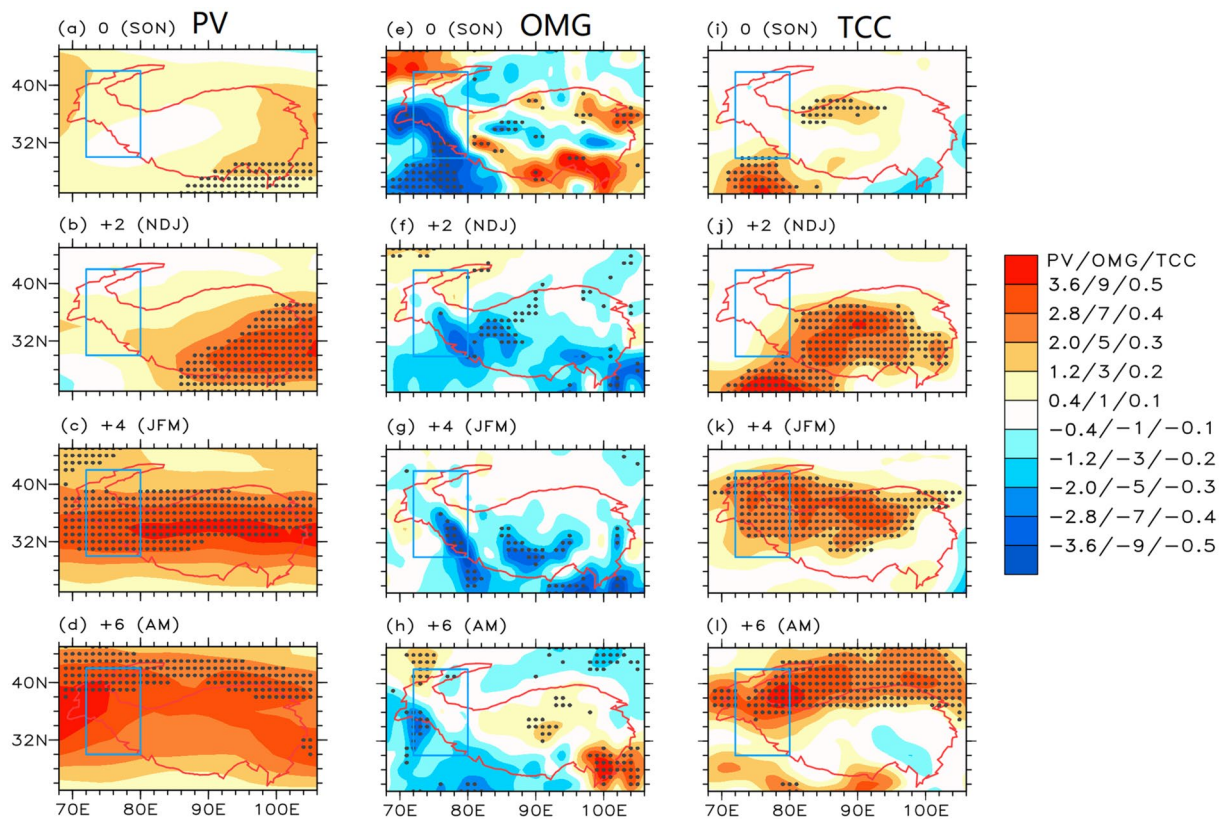
Fig. 12 Spatial distribution of the linear regression maps of **a–d** SCE (unit: %) and **e–h** snow depth (unit: m 10^{-5}) on the ASI for the period 1979–2015 for **a, e** SON, **b, f** NDJ, **c, g** JFM and **d, h** AM. Correlation coefficients significant at the 95% level are dotted

Figure 15 presents the ASI-related geopotential height anomalies at 200 hPa from autumn to the following spring, and the corresponding WAF values are overlaid as vectors. In association with the positive WTP snow cover, negative geopotential height anomalies appear (Fig. 15a). These negative geopotential height anomalies intensify and expand with time. Two months later, this anomalously low system is centered over the eastern TP (Fig. 15b). This anomalously low system strengthens with time and propagates northeastward. It combines with another negative geopotential height anomaly over the extratropical North Pacific and forms a wide band of significant negative geopotential height anomalies between 30° N and 60° N, dominating EA–western North Pacific regions in late winter (Fig. 15c). In the following spring, the band of significant negative geopotential height anomalies weakens and is mostly confined north of 40° N (Fig. 15d). A branch of the WAF is also observed propagating southeastward from the negative geopotential height anomalies around southeastern Lake Baikal and reaching midlatitude coastal EA, contributing to the formation of a positive anomalously high system centered over eastern Japan (Fig. 15d). The geopotential height anomalies over coastal EA and the western North Pacific cause weakening and northward changes in the EASJ, as shown in Fig. 9. The changes in the EASJ induce upper-level divergence and low-level convergence together with the ascent motion around coastal EA, thus favoring a positive anomalous SPSC.

Fig. 13 **a** Spatial distribution of the linear regression maps of (**a**–**d**) potential vorticity (unit: $10^{-8} \times \mathrm{K} \cdot \mathrm{m}^2/\mathrm{kg/s}$) at 200 hPa, **e**–**h** vertical velocity (unit: $10^{-4} \times \mathrm{pa/s}$ at 200 hPa and **i**–**l** total cloud cover (TCC) (unit: %) onto the ASI for the period 1979–2015 for **a**, **e**, **i** SON, **b**, **f**, **j** NDJ, **c**, **g**, **k** JFM and **d**, **h**, **l** AM. Correlation coefficients significant at the 95% level are dotted

5 Conclusions

The western TP has large climatological snow amounts, and the largest snow variation occurs in autumn. The current study revealed that the snow cover anomalies over the WTP in autumn can significantly impact variations in the SPSC. When more ASC occurs over the WTP, the precipitation over southern China tends to be anomalously high in the following spring. The positive correlation between variations in the ASC and the SPSC is independent of the tropical Indo-Pacific SST influence. The analysis results show that when positive ASC anomalies occur over the WTP, pronounced negative and positive geopotential height anomalies dominate the eastern EA-western North Pacific region in the following spring. In southern China and nearby areas, anomalous southerly winds prevail, and they induce water vapor from the tropical ocean northward to the interior of the continent, which can cause moisture convergence and promote positive SPSC. Meanwhile, the EASJ is weakened and shifts northward; consequently, anomalous upper-level divergence and low-level convergence patterns are observed along with anomalous ascending motion that dominates coastal EA and nearby regions,

thereby promoting positive SPSC anomalies over these areas.

An analysis of the local energy budget reveals that local positive snow-air feedback helps maintain the snow anomalies over the WTP from autumn to the following spring. More specifically, when there is anomalous positive ASC over the WTP, the net impact of snow on the above atmosphere produces a cooling effect. Associated with this cooling, low geopotential height anomalies appear above the plateau. The upper-level negative geopotential height anomalies and cold temperatures favor an increase in the upper potential vorticity. Anomalous ascent motions follow, which leads to increased snowfall over the WTP and is favorable for the persistence of snow. The current work revealed a cross-season snow-precipitation relationship, with changes in the autumn TP snow leading to variations in the SPSC for two seasons. This finding might provide useful information and an additional potential predictor for seasonal prediction of the SPSC.

In the current work, we focus on examining the forcing effect of the underlying autumn TP snow on the above atmosphere in the following winter and spring. The anomalous autumn TP snow itself is possibly influenced

Fig. 14 Regression map of the geopotential height (unit: m, shading) and wind (vector, unit: m/s) on ASI for the period 1979–2015 along 32.5° N for **a** SON, **b** NDJ and **c** JFM. The gray shading represents the topography. The dotted regions represent height anomalies significant at the 95% confidence level
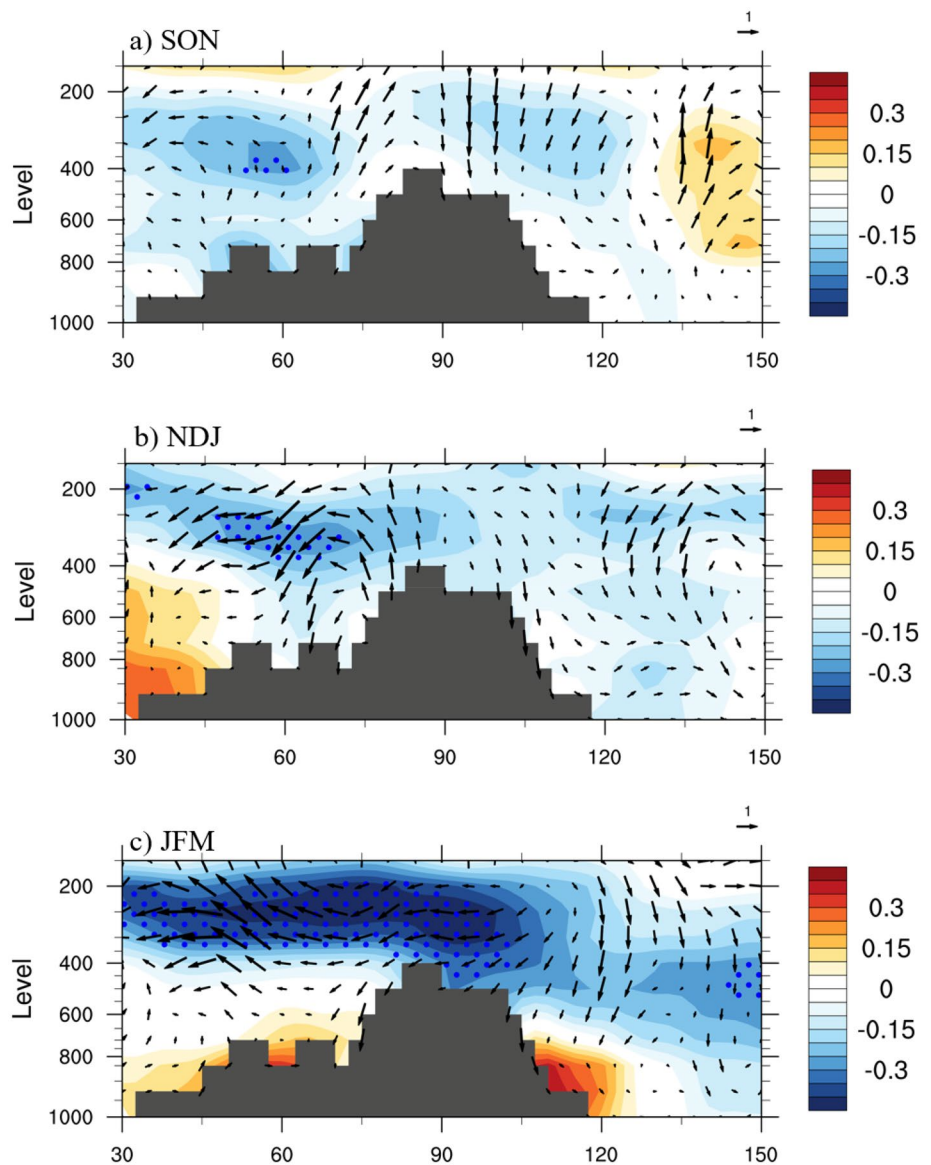
by remote atmospheric circulation (e.g., Qian et al. 2019). As shown by Fig. 15a, positive height anomalies occur upstream of the western TP. The anomalous North Atlantic SST in the previous seasons associated with ASI is calculated using regression (not shown), and significant SSTAs can be observed in the North Atlantic, which can be tracked back to the previous summer. The results imply a possible link between North Atlantic summer SSTAs-Eurasian atmospheric wave train-western TP autumn snow anomalies. In summary, the western TP snow anomalies may be first impacted by the North Atlantic SST anomalies from previous seasons through remote atmospheric circulations. The western TP snow anomalies then positively feed back to the atmosphere and impact the SPSC in the following spring.

Fig. 15 Spatial distribution of the linear regression map of the Z200 (contour, unit: m) and wave activity flux (vector, unit: m²/s⁻²) for **a** SON, **b** NDJ, **c** JFM and **d** AM on the ASI for the period 1979–2015. The dotted regions represent anomalies significant at the 95% confidence level
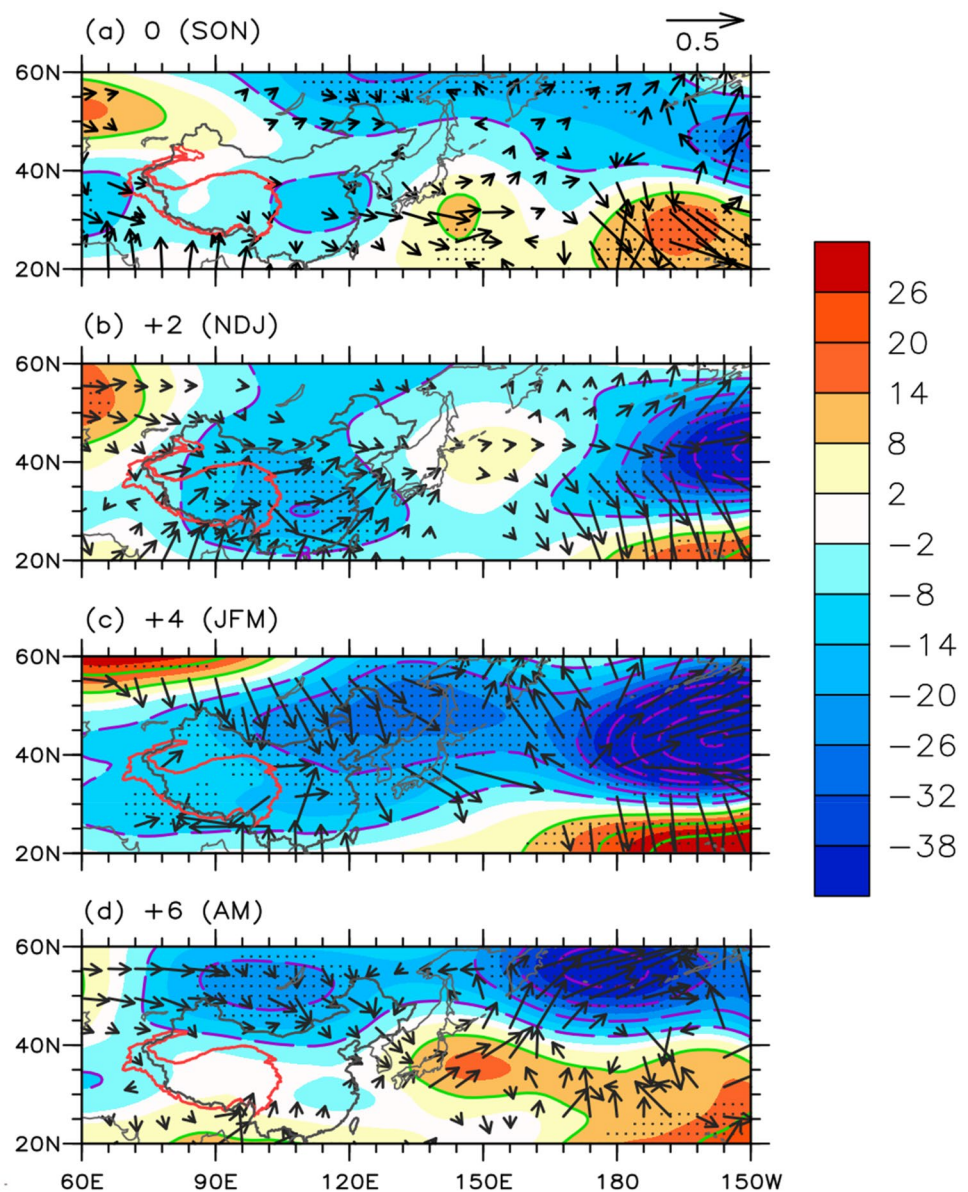
References

Barnett TP, Dumenil L, Schlese U et al (1989) The effect of Eurasian snow cover on regional and global climate variations. J Atmos Sci 46(5):661–685. https://doi.org/10.1175/1520-0469(1989)046%3c0661:TEOESC%3e2.0.CO;2

Berrisford P, Dee D, Poli P et al (2011) The ERA-interim archive. ERA report series, 1, ECMWF, Shinfield Park, Reading. https://old.ecmwf.int/publications/library/do/references/show?id=90276

Cai X, Wang V, Xu J (2002) Diagnostic analysis on impact of convective activity anomalies over tropic on flood/drought during the first rainy season in south China. J Trop Meteorol 18(2):158–161. https://doi.org/10.1002/mop.10502 (**in Chinese**)

Chang CP, Zhang Y, Li T (2000) Interannual and interdecadal variations of the East Asian summer monsoon and tropical Pacific SSTs. Part I: roles of the subtropical ridge. J Clim 13:4310–4325. https://doi.org/10.1175/1520-0442(2000)013,4310:IAIVOT.2.0.CO;2

Chen Y, Qian Y (2005) Numerical study of influence of the SSTA in western Pacific warm pool on precipitation in the first flood period in south China. J Trop Meteorol 21(1):13–23 (**in Chinese**)

Chen S, Wang Q, Qian Y (2003) Preliminary discussions of basic climatic characteristics of precipitation during raining seasons in regions south of Changjiang River and its relationship with SST anomalies. J Trop Meteorol 19(3):260–268. https://doi.org/10.3969/j.issn.1006-8775.2003.02.010 (**in Chinese**)

Chen W, Feng J, Wu R (2013) Roles of ENSO and PDO in the link of the East Asian winter monsoon to the following summer monsoon. J Clim 26:622–635. https://doi.org/10.1175/JCLI-D-12-00021.1

Chen JP, Wen ZP, Wu RG et al (2014) Interdecadal changes in the relationship between southern China winter-spring precipitation and ENSO. Clim Dyn 43(5–6):1327–1338. https://doi.org/10.1007/s00382-013-1947-x

Dash SK, Singh GP, Shekhar MS et al (2005) Response of the Indian summer monsoon circulation and rainfall to seasonal snow depth anomaly over Eurasia. Clim Dyn 24(1):1–10. https://doi.org/10.1007/s00382-004-0448-3

Dickson RE (1984) Eurasian snow cover versus Indian monsoon rainfall—an extension of the Hahn-Shukla results. J Clim Appl Meteorol 23:171–173. https://doi.org/10.1175/1520-0450(1984)023%3c0171:ESCVIM%3e2.0.CO;2

Dou J, Wu Z (2018) Southern Hemisphere origins for interannual variations of Tibetan Plateau snow cover in boreal summer. J Clim 31:7701–7718. https://doi.org/10.1175/JCLI-D-17-327.1

Feng J, Li J (2011) Influence of El Niño Modoki on spring rainfall over south China. J Geophys Res Atmos 116:D13102. https://doi.org/10.1029/2010JD015160

Gu W, Wang L, Hu Z, Hu K et al (2018) Interannual variations of the first rainy season precipitation over South China. J Clim 31(2):623–640. https://doi.org/10.1175/JCLI-D-17-0284.1

Hahn DG, Shukla J (1976) An apparent relationship between Eurasian snow cover and Indian monsoon rainfall. J Atmos Sci 33:2461–2462. https://doi.org/10.1175/1520-0469(1976)033%3c2461:AARBES%3e2.0.CO;2

Immerzeel WW, van Beek LPH, Bierkens MFP (2010) Climate change will affect the Asian water towers. Science 328(5984):1382–1385. https://doi.org/10.1126/science.1183188

Jia XJ, Cao D, Ge JW et al (2018) Interdecadal change of the impact of Eurasian snow on spring precipitation over southern China. J Geophys Res Atmos 123(18):10092–10108. https://doi.org/10.1029/2018JD028612

Jia XJ, You YJ, Wu R et al (2019) Interdecadal changes in the dominant modes of the interannual variation of spring precipitation over china in the mid-1980s. J Geophys Res 124(20):10676–10695. https://doi.org/10.1029/2019JD030901

Jin R, Wu Z, Zhang P (2018) Tibetan Plateau capacitor effect during the summer preceding ENSO: from the Yellow River climate perspective. Clim Dyn 51(1):57–71. https://doi.org/10.1007/s00382-017-3906-4

Khandekar ML (1991) Eurasian snow cover, Indian monsoon and El Nino/Southern Oscillation-a synthesis. Atmos Ocean 29(4):636–647. https://doi.org/10.1080/07055900.1991.9649422

Kripalani RH, Kulkarni A (1999) Climatology and variability of historical Soviet snow depth data: some new perspectives in snow-Indian monsoon tele-connections. Clim Dyn 15:475–489. https://doi.org/10.1007/s003820050294

Kripalani RH, Kim BJ, Oh J et al (2002) Relationship between Soviet snow and Korean rainfall. Int J Climatol 22:1313–1325. https://doi.org/10.1002/joc.809

Lau KM, Li TM (1984) The monsoon of East Asia and its global associations—a survey. Bull Am Meteorol Soc 65:114–125. https://doi.org/10.1175/1520-0477(1984)065,0114:TMOEAA.2.0.CO;2

Lin H, Wu Z (2011) Contribution of the autumn Tibetan Plateau snow cover to seasonal prediction of North American winter temperature. J Clim 24(11):2801–2813. https://doi.org/10.1175/2010JCLI3889.1

Lin H, Wu Z (2012) Contribution of Tibetan Plateau snow cover to the extreme winter conditions of 2009/10. Atmos Ocean 50(1):86–94. https://doi.org/10.1080/07055900.2011.649036

Liu G, Wu RG, Zhang Y et al (2014) The summer snow cover anomaly over the Tibetan Plateau and its association with simultaneous precipitation over the Meiyu-Baiu region. Adv Atmos Sci 31(4):755–764. https://doi.org/10.1007/s00376-013-3183-z

Lyu M, Wen M, Wu Z (2018) Possible contribution of the interannual Tibetan Plateau snow cover variation to the Madden-Julian Oscillation convection variability. Int J Climatol 38:3787–3800

Qian QF, Jia XJ, Wu RG (2019) Changes in the impact of the Autumn Tibet Plateau snow cover on the Winter temperature over North America in the mid-1990s. J Geophys Res Atmos. https://doi.org/10.1029/2019JD030245

Rayner NA, Parker DE, Horton EB et al (2003a) Global analyses of sea surface temperature, sea ice, and night marine air temperature since the late nineteenth century. J Geophys Res Atmos 108(D14):4407. https://doi.org/10.1029/2002JD002670

Rayner NA, Parker DE, Horton EB et al (2003b) Global analyses of sea surface temperature, sea ice, and night marine air temperature since the late nineteenth century. J Geophys Res 108:D14. https://doi.org/10.1029/2002JD002670

Robinson DA, Estilow TW, Program NOAACDR (2012) NOAA Climate Data Record (CDR) of Northern Hemisphere (NH) Snow Cover Extent (SCE), version 1. NOAA Natl Cent Environ Inf. https://doi.org/10.7289/V5N014G9

Singh GP, Oh JH (2005) Study on snow depth anomaly over Eurasia, Indian rainfall and circulations. J Meteorol Soc Jpn 83(2):237–250. https://doi.org/10.2151/jmsj.83.237

Takaya K, Nakamura H (2001) A formulation of a phase-independent wave-activity flux for stationary and migratory quasigeostrophic eddies on a zonally varying basic flow. J Atmos Sci 58(6):608–627. https://doi.org/10.1175/1520-0469(2001)058%3c0608:AFOAPI%3e2.0.CO;2

Wang B, Wu R, Fu X (2000) Pacific-East Asian teleconnection: how does ENSO affect East Asian climate? J Clim 13(9):1517–1536. https://doi.org/10.1175/1520-0442(2000)013%3c1517:PEATHD%3e2.0.CO;2

Wang B, Wu R, Li T (2003) Atmosphere-warm ocean interaction and its impacts on Asian–Australian monsoon variation. J Clim 16(8):1195–1211. https://doi.org/10.1175/1520-0442(2003)16%3c1195:AOIAII%3e2.0.CO;2

Wang Z, Wu R, Huang G (2017) Low-frequency snow changes over the Tibetan Plateau. Int J Climatol 38(2):949–963. https://doi.org/10.1002/joc.5221

Wang Z, Wu R, Chen S et al (2018) Influence of western Tibetan Plateau summer snow cover on East Asian summer rainfall. J Geophys Res Atmos 123(5):2371–2386. https://doi.org/10.1002/2017JD028016

Wang M, Jia XJ, Ge JW et al (2019) Changes in the relationship between the interannual variation of Eurasian snow cover and spring SAT over Eastern Eurasia. J Geophys Res Atmos 124(2):468–487. https://doi.org/10.1029/2018JD029077

Wang Z, Wu R, Zhao P et al (2019) Formation of snow cover anomalies over the Tibetan Plateau in cold seasons. J Geophys Res Atmos 124(9):4873–4890. https://doi.org/10.1029/2018JD029525

Watanabe M, Kimoto M (2000) Atmosphere-ocean thermal coupling in the North Atlantic: a positive feedback. Q J R Meteorol Soc 126:3343–3369. https://doi.org/10.1002/qj.49712657017

Watanabe M, Nitta T (1998) Relative impacts of snow and sea surface temperature anomalies on an extreme phase in the winter atmospheric circulation. J Clim 11(11):2837–2857. https://doi.org/10.1175/1520-0442(1998)011%3c2837:RIOSAS%3e2.0.CO;2

Wu R, Chen S (2016) Regional change in snow water equivalent–surface air temperature relationship over Eurasia during boreal spring. Clim Dyn 47:2425–2442. https://doi.org/10.1007/s00382-015-2972-8

Wu R, Kirtman BP (2007) Observed relationship of spring and summer East Asian rainfall with winter and spring Eurasian snow. J Clim 20:1285–1304. https://doi.org/10.1175/JCLI4068.1

Wu R, Hu Z, Kirtman BP (2003) Evolution of ENSO-related rainfall anomalies in East Asia. J Clim 16:3742–3758. https://

doi.org/10.1175/1520-0442(2003)016%3c3742:EOERA I%3e2.0.CO;2

Wu Q, Hu H, Zhang L (2011) Observed influences of autumn–early winter Eurasian snow cover anomalies on the hemispheric PNA-like variability in winter. J Clim 24(7):2017–2023. https://doi.org/10.1175/2011JCLI4236.1

Wu Z, Jiang Z, Li J et al (2012) Possible association of the western Tibetan Plateau snow cover with the decadal to interdecadal variations of Northern China heatwave frequency. Clim Dyn 39:2393–2402. https://doi.org/10.1007/s00382-012-1439-4

Wu Z, Li J, Jiang Z et al (2012) Modulation of the Tibetan Plateau Snow Cover on the ENSO teleconnections: from the east Asian Summer monsoon perspective. J Clim 25:2481–2489. https://doi.org/10.1175/JCLI-D-11-00135.1

Wu Z, Zhang P, Chen H et al (2016) Can the Tibetan Plateau snow cover influence the interannual variations of Eurasian heat wave frequency? Clim Dyn 46:3405–3417. https://doi.org/10.1007/s00382-015-2775-y

Xie S, Hu K, Hafner J et al (2009) Indian Ocean capacitor effect on Indo-western Pacific climate during the summer following El Niño. J Clim 22(3):730–747. https://doi.org/10.1175/2008JCLI2544.1

Yang S, Lau KM, Kim KM (2002) Variations of the East Asian jet stream and Asian-Pacific-American winter climate anomalies. J Clim 15:306–325. https://doi.org/10.1175/1520-442(2002)015%3c0306:VOTEAJ%3e2.0.CO;2

Yeh T, Gao Y (1979) Meteorology of the Qinghai-Xizang (Tibet) Plateau. Science Press, Beijing (**in Chinese**)

Ye K, Wu R, Liu Y (2015) Interdecadal change of Eurasian snow, surface temperature, and atmospheric circulation in the late 1980s. J Geophys Res Atmos 120:2738–2753. https://doi.org/10.1002/2015JD023148

Yim S, Jhun J, Lu R et al (2010) Two distinct patterns of spring Eurasian snow cover anomaly and their impacts on the East Asian summer monsoon. J Geophys Res Atmos 115:D22113. https://doi.org/10.1029/2010JD013996

You Y, Jia XJ (2018) Interannual variations and prediction of spring precipitation over China. J Clim 31:655–670. https://doi.org/10.1175/JCLI-D-17-0233.1

Zhang YS, LiT WB (2004) Decadal change of the spring snow depth over the Tibetan Plateau: the associated circulation and influence on the East Asian summer monsoon. J Clim 17:2780–2793. https://doi.org/10.1175/1520-0442(2004)017%3c2780:DCOTSS%3e2.0.CO;2

Zuo Z, Zhang R, Wu B et al (2012) Decadal variability in springtime snow over Eurasia: relation with circulation and possible influence on springtime rainfall over China. Int J Climatol 32(9):1336–1345. https://doi.org/10.1002/joc.2355